

Dynamic Modeling of Damping Effects in Highly Damped Compliant Fingers for Applications Involving Contacts

Chih-Hsing Liu

Singapore Institute of Manufacturing Technology,
Singapore 638075
e-mail: chliu@simtech.a-star.edu.sg

Kok-Meng Lee¹

The George W. Woodruff School of
Mechanical Engineering,
Georgia Institute of Technology,
Atlanta, GA 30332-0405
e-mail: kokmeng.lee@me.gatech.edu

In many industries, it is often required to transfer objects using compliant fingers capable of accommodating a limited range of object shapes/sizes without causing damage to the products being handled. This paper presents a coupled computational and experimental method in time domain to characterize the damping coefficient of a continuum structure, particularly, its applications for analyzing the damping effect of a highly damped compliant finger on contact-induced forces and stresses. With the aid of Rayleigh damping and explicit dynamic finite element analysis (FEA), this method relaxes several limitations of commonly used damping identification methods (such as log-decrement and half-power methods) that are valid for systems with an oscillatory response and generally estimate the damping ratio for a lumped parameter model. This damping identification method implemented using off-the-shelf commercial FEA packages has been validated by comparing results against published data; both oscillatory and nonoscillatory responses are considered. Along with a detailed discussion on practical issues commonly encountered in explicit dynamic FEA for damping identification, the effects of damping coefficients on contact between a rotating compliant finger and an elliptical object has been numerically investigated and experimentally validated. The findings offer a better understanding for improving grasper designs for applications where joint-less compliant fingers are advantageous. [DOI: 10.1115/1.4005270]

Keywords: damping, flexible mechanism, rotating finger, compliant finger, finite element, multibody dynamics

1 Introduction

Compliant mechanisms that transfer force, motion, and energy through elastic deformations offer several advantages in food-product handling applications where designs must accommodate a limited range of object sizes and shapes. Most existing dynamic analyses of compliant multibody systems are based on quasi-static lumped parameter models without considering the effects of damping. However, damping effects play an important role in mechanical handling of natural and/or live products at high production speed; therefore, it is desirable to have a good understanding of the damping effect on the contact-induced forces and stresses in order to facilitate the design of a flexible multibody dynamic system.

This paper is motivated by the need to analyze dynamic performances of compliant fingers in order to reduce the number of design configurations and live broilers (meat chickens) needed in developing an automated live-bird transfer system [1] for the poultry meat processing industry. A fundamental task is the design and control of mechanical “hands” with rotating compliant fingers, which offer several advantages including light weight, no relative moving parts (hence, less expensive to manufacture), and most importantly, the flexibility to accommodate a limited range of sizes/shapes and natural reactions without causing damage to products. To overcome limitations of lumped parameter models such as pseudo-rigid-body models [2,3] that treat flexible members as rigid links with torsional pin-joints, Lee et al. [4] performed a parametric study using 2D finite element analysis (FEA)

on contact forces acting on an object. Several other analytical models [5,6] have also been developed to predict the contact force and deflected shape of compliant fingers. These studies generally model the finger as a 2D beam and analyze the finger dynamics quasi-statically without considering damping effects.

Damping, which dissipates energy and causes vibration to decay with time, is often characterized by a damping ratio (defined as the ratio of actual to critical viscous damping). To obtain the damping parameters, time, or frequency domain experiments are usually required. In time domain, damping ratios are determined from logarithmic decrements; for examples, free vibration of steel poles and tubular towers measured by accelerometers [7]; and impulse response of a wire cable [8] captured using a high-speed digital camera. Damping ratios can also be calculated from the half-power bandwidth of a measured frequency response; for example, the frequency response of a gearbox measured with a laser vibrometer in Ref. [9]. These damping identification methods (based on log-decrement or half-power bandwidth) that estimate the damping ratios for lumped parameter models are only valid for lightly damped structures exhibiting overshoots. Rayleigh damping (also known as proportional damping) is often used in mathematical models for simulating the dynamic response of a structure (for examples, Refs. [8,10]). Expressed as a linear combination of terms proportional to the stiffness and mass of the structure, Rayleigh damping avoids the need to form a damping matrix based on the physical properties of the real structure in numerical analyses. To better understand the damping effect on the reaction forces and stresses due to contact, we investigate the use of three-dimensional (3D) explicit dynamic FEA methods for modeling the dynamics of a flexible multibody system with large deformations and contact nonlinearities. The remainder of this paper offers the following:

¹Corresponding author.

Contributed by the Dynamic Systems Division of ASME for publication in the JOURNAL OF DYNAMIC SYSTEMS, MEASUREMENT AND CONTROL. Manuscript received July 2, 2010; final manuscript received July 31, 2011; published online December 2, 2011. Assoc. Editor: Luis Alvarez.

- (1) A coupled computational and experimental damping identification (CCEDI) method, which models the damping of a highly damped flexible member in the time domain for numerical analysis, is presented. This method relaxes several limitations on log-decrement or half-power methods that are only applicable for systems with an oscillatory response and generally estimate the damping ratio for a lumped parameter model. This CCEDI method with Rayleigh damping is able to obtain the damping coefficient of a continuum structure. As will be shown, Rayleigh damping reduces to a single mass proportional term for low-frequency applications where the stiffness proportional term is insignificant. Based on this approach, the critical damping coefficient can be obtained numerically and the damping coefficient of a highly damped structure can be estimated with the aid of experimental data.
- (2) The CCEDI method can be implemented using off-the-shelf general-purpose numerical packages. In this paper, the numerical packages ANSYS, LS-DYNA, and LS-PREPOST are used for preprocessing, solving, and postprocessing, respectively, where the nodal coordinate and element data are numerically programmed by the ANSYS Parametric Design Language (APDL) and output as a text file; and the discrete finite element (FE) equations of motion, along with the defined boundary conditions and contact algorithm, are solved using LS-DYNA. The CCEDI method has been validated by comparing results against published data. Under-damped and over-damped cases are both discussed.
- (3) Practical issues encountered in dynamic FEA based on explicit time-integration methods are discussed. Compared to implicit methods which are stable for linear and many nonlinear problems, explicit methods are computationally less expensive since no matrix inversion is required in each time-step. However, explicit methods are only stable when the time-step is smaller than a critical size known as the Courant–Friedrichs–Levy (CFL) condition [11,12]; and thus, the time-step size is a compromise between numerical stability and computation time.
- (4) The effect of different damping coefficients on the contact between a rotating finger and an elliptical object is numerically investigated and discussed. The findings provide a means for improving grasper designs and for applications where joint-less compliant fingers are advantageous.

2 FEA-based Damping Model Consideration

The discrete equations of motion for FEA can be derived from the work balance contributed by the external load, inertial effect, viscosity, and strain energy. The computational model for the system is outlined in Appendix A

$$[M]\{\ddot{X}\} + [C]\{\dot{X}\} + [K]\{X\} = \{F\} \quad (1)$$

where $\{X\}$ is the global nodal degree of freedom (DOF); $\{F\}$ is the load vector; and $[M]$, $[C]$, and $[K]$ are the global mass, damping, and stiffness matrices, respectively. ANSYS and LS-DYNA (with a built-in penalty method to handle deformable contacts) are used to create the discrete domain $\{X\}$, and solve Eq. (1) using an explicit FEA method, respectively. In this paper, Rayleigh (proportional) damping is assumed

$$[C] = \alpha[M] + \beta[K] \quad (2)$$

where the mass and stiffness matrices, $[M]$ and $[K]$ defined in Eq. (1), can be formulated once the element types are defined. The relative effect of the coefficients α and β on the effective damping ratio ζ can be illustrated with a classical single-DOF system (mass m and spring k with damper written as $c = \alpha m + \beta k$), where the natural frequency ω_n and damping ratio ζ are written as

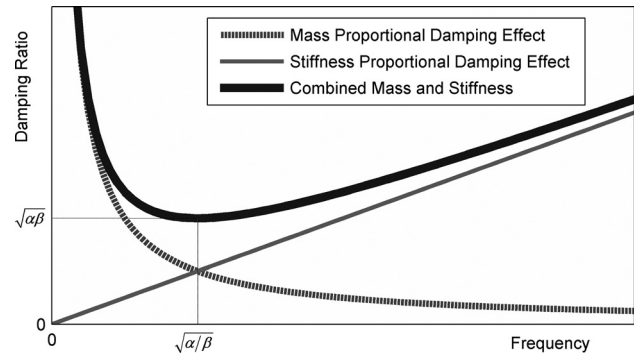


Fig. 1 Frequency effect of proportional damping on damping ratio

$$\omega_n^2 = \frac{k}{m} \quad (3a)$$

$$\zeta = \frac{c}{c_{cr}} = \frac{1}{2} \left(\frac{\alpha}{\omega_n} + \beta \omega_n \right) \quad (3b)$$

Based on Eq. (3b), the proportional damping effect is illustrated in Fig. 1 showing that the mass proportional damping term heavily damps the lowest modes and dominates in low-frequency applications. The opposite effect can be observed for the stiffness proportional damping term which damps the modes at high frequencies. The effect can be illustrated numerically with the following example:

2.1 Numerical Example. Considering the frequency range from ω_1 to ω_2 (with corresponding damping ratios ζ_1 and ζ_2), the mass and stiffness proportional coefficients α and β can be solved from the simultaneous equations from Eq. (3b)

$$\alpha = 2\omega_1\omega_2 \frac{\zeta_1\omega_2 - \zeta_2\omega_1}{\omega_2^2 - \omega_1^2} \quad (4a)$$

$$\beta = 2 \frac{\zeta_2\omega_2 - \zeta_1\omega_1}{\omega_2^2 - \omega_1^2} \quad (4b)$$

As an illustration, consider $\omega_1 = 2\pi(10)$ rad/s, $\omega_2 = 2\pi(20)$ rad/s, and $\zeta_1 = \zeta_2 = 0.1$, thus $\alpha/\beta = 8.38 \times 10^3 \text{ s}^{-2}$. The above implies that the stiffness proportional β term is insignificant for structures in the low-frequency modes.

For low-frequency applications, the coefficient α can be determined using a coupled computational and experimental damping identification (CCEDI) method as illustrated in Fig. 2. This procedure combines explicit dynamic FEA, mass proportional damping assumption, and traditional damping identification from oscillatory response data to determine α . For an over-damped structure, the procedure numerically searches for the damping coefficient by comparing the solution to Eq. (1) based on an initial α against experimentally measured (impulse response) data until a match is found. For an under-damped case, the damping coefficient is simply the product of α_{cr} and ζ ; the latter can be experimentally obtained using traditional methods, and thus, the procedure searches for the critical mass proportional coefficient α_{cr} between oscillation and nonoscillation responses by numerically solving Eq. (1). The advantages of this damping identification technique are its capability to analyze highly damped continuum structures and obtain the damping coefficients for FEA.

2.2 Illustrative Example: Lightly Damped Compliant Beam with Tip Mass. The free vibration of a compliant cantilevered steel rod (0.4 m length, 0.6 mm diameter, and 0.9 g mass) with a tip mass (0.015 g) at its free-end is simulated to illustrate the damping identification, where the tip response data (experimentally measured by a high-speed camera) are available given in

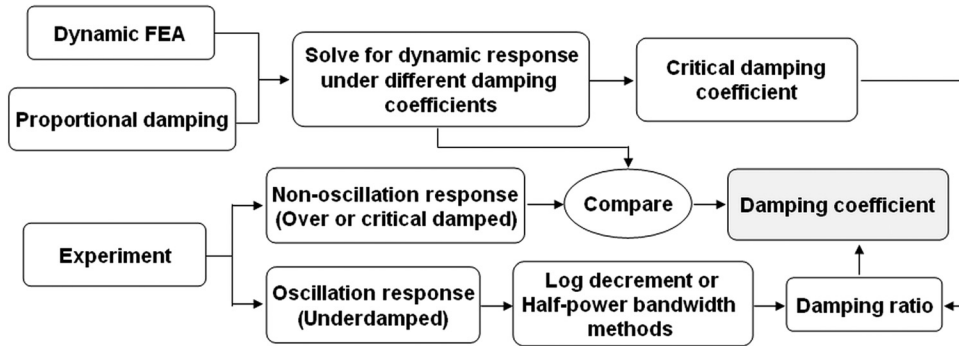


Fig. 2 Coupled computational and experimental damping identification (CCEDI) method

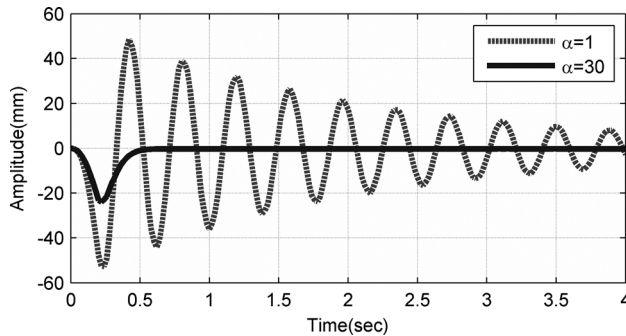


Fig. 3 Impulse response with initial guessed and critical damping coefficients ($\alpha_{cr} = 30 \text{ s}^{-1}$, $\zeta = 0.0055$)

Ref. [13] for validation. From the published experimental response, the damping ratio ζ and natural frequency ω_n are found to be 0.0055 and 16.33 rad/s, respectively. Although the single-DOF lumped parameter model has an advantage of offering the dynamic behavior of the end-point by simply treating the system as a “black box,” it cannot be used to calculate any contact and stress-strain relation along the beam.

Since the compliant beam vibrates at its 1st mode, the stiffness proportional damping term is neglected. The critical mass proportional damping coefficient α_{cr} is found using the CCEDI procedure. Meshed in ANSYS (with the elements defined in Appendix B), the tip response of the steel compliant beam (density $\rho = 7957 \text{ kg/m}^3$ and Young’s modulus $E = 209 \text{ GPa}$) to an impulse loading (0.003 N, for 0.2 s) is simulated by solving Eq. (1) using LS-DYNA. With the compliant beam and tip mass modeled using the BEAM161 element (100 elements and 101 nodes) and MASS166 element (1 element and 1 node) in ANSYS, respectively, the impulse response of the tip for a specified α can be computed. BEAM161 and MASS166 in ANSYS correspond to Beam Element 1 and Mass Element 2 for element transformation to LS-DYNA. Using the log-decrement method to analyze the decaying amplitudes in the iterative search, the critical damping coefficient was found to be $\alpha_{cr} = 30 \text{ s}^{-1}$. Thus, $\alpha = \alpha_{cr}\zeta = 0.165 \text{ s}^{-1}$, which can be used in dynamic FEA. Figure 3 shows the impulse responses computed with the initial-guessed and critical damping coefficients. The FEA simulated tip response is compared against published experimental results in Fig. 4, which shows excellent agreement.

3 Results and Discussion

We discuss the effects of key design parameters on the damping of a continuum structure and relevant implementation issues in the context of a compliant finger (Fig. 5(a)) commonly used in live broiler handling and processing applications [1,4], where contact-induced forces and stresses exerted by rotating fingers on an object are of concern. Detailed in Fig. 5(a), the compliant finger consists of evenly spaced elliptical ribs along with the rein-

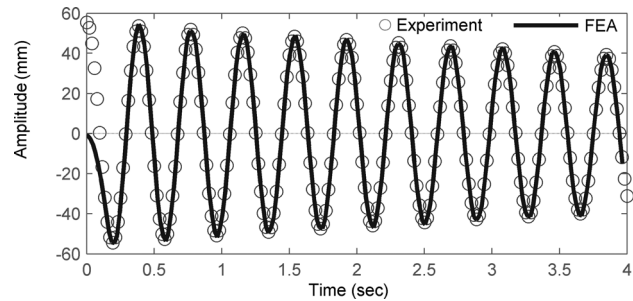


Fig. 4 Comparison of simulation and published experimental data ($\alpha = \alpha_{cr}\zeta = 0.165 \text{ s}^{-1}$)

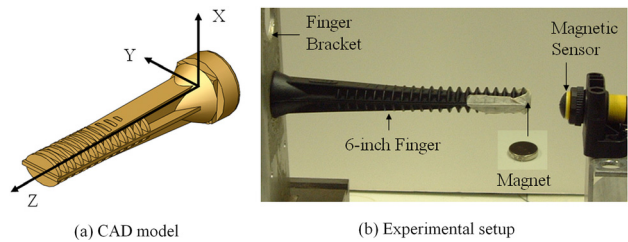


Fig. 5 Setup for damping identification of the compliant finger

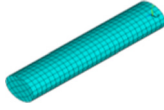
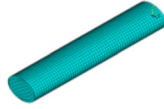
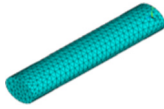
forced structure making up of a thin horizontal plate, a cone, and a rectangular section tapering from the fixed circular end (of 17.5 mm radius). The finger is designed to bend easily in the XZ plane but relatively rigid in other planes. Figure 5(b) shows the setup for this study, where the tested rubber finger (model WK52H manufactured by the Waukesha Rubber Company) is clamped at one end and an impulse load is applied at the other end. A cylindrical (4 mm-radius and 1.65 mm-thick) permanent magnet is embedded in the fingertip such that the tip displacements can be determined from the magnetic field measured by a (Banner S18MB) magnetic sensor.

The following discusses the results of four specific studies; namely, (1) effects of geometric complexity on FEA computation for damping identification; (2) effectiveness of the CCEDI method; (3) method validation against previously published experimental data; and (4) effects of damping on reaction forces/stresses.

3.1 Numerical Investigation of the Effect of Geometrical Models on FEA Computation for the Damping Coefficients.

The CCEDI method for determining the damping coefficient, though straight-forward, is computationally time-consuming. Explicit time-integration that determines the next time-step unknowns in terms of previously computed quantities is used in order to avoid inverting stiffness matrix in each time-step and thus reduce

Table 1 Different FEM models of a 4.5-in. compliant finger

	Rubber finger	Element type ^a	Time step
FEM models	E = 6.1 MPa	Average length	Step size (μ s)
volume	$\nu = 0.49$	# of nodes	# of steps to 0.2 s
equivalent stiffness	$\rho = 1000 \text{ kg/m}^3$	# of elements	Step ratio (relative to SM-A)
Detailed model (DM)		Tetra	
30 cm ³		2.8 mm	0.22
81.2 N/m		36782	909091
		23147	18.36
Simplified model A (SM-A)		Hexa	
36 cm ³		4 mm	4.04
73.8 N/m		1080	49505
		725	1
Simplified model B (SM-B)		Refined hexa	
36 cm ³		2 mm	1.43
74.0 N/m		5900	139860
		4698	2.83
Simplified model C (SM-C)		Tetra	
36 cm ³		4 mm	1.26
74.9 N/m		7481	158730
		4682	3.21

^aDefined in Appendix B.

computational time. Although computationally efficient, the time-step Δt of explicit FEA must satisfy the CFL condition (that depends on element types/shapes as well as material properties [11]) to ensure numerical stability [12,14].

To study the effect of geometry and element types on the computational time, three simplified FE models (SM-A, B, and C) against the detailed model (DM) are compared in Table 1 where for simplicity the acronyms “hexa” and “tetra” refer to three-dimensional 8-node hexagonal and 10-node tetrahedral elements, respectively. The description of hexagonal and tetrahedral elements can be found in Appendix B. All three simplified models have the same constant elliptical cross-section (major and minor radii of 12 mm and 8.45 mm, respectively) throughout the length but are meshed with different element sizes and/or shapes. In Table 1, the equivalent stiffness is computed from the force-displacement relationship at the free-end using the nonlinear static FEA by ANSYS, where two known loads (1 N and 2 N) were used to determine the average equivalent stiffness.

For stability consideration, the numerical time-step must be smaller than the critical time-step which is the smallest value in the global analysis domain (and thus, it is desirable to have a uniform mesh in explicit FEA):

$$\Delta t_{\text{num}} = a \times \min\{\Delta t_1, \Delta t_2, \dots, \Delta t_n\} \quad (5)$$

where a is the scale factor between 0 and 1, and defined as 0.9 in this study. The critical time-step calculations for tetrahedral and hexahedral solid elements can be found in Ref. [11], and are given here for completeness

$$\Delta t = \frac{L_e}{[Q + \sqrt{Q^2 + c_w^2}]} \quad \text{where } c_w = \sqrt{\frac{E(1-\nu)}{\rho(1+\nu)(1-2\nu)}},$$

$$Q = \begin{cases} C_1 c_w + C_0 L_e |\dot{\epsilon}|, & \dot{\epsilon} < 0 \\ 0, & \dot{\epsilon} \geq 0 \end{cases}, \quad \text{and}$$

$$L_e = \begin{cases} V_e / A_{\text{emax}}, & \text{hexahedral} \\ \text{minimum altitude}, & \text{tetrahedral} \end{cases} \quad (6)$$

In Eq. (6), Q is a function of the bulk viscosity coefficients C_0 and C_1 ; $\dot{\epsilon}$ is the strain rate; V_e is the volume of the element; and A_{emax} is the area for the largest side of the element. The effects of critical time-steps on the computation time are illustrated in the last column of Table 1, where “# of steps to 0.2 s” intuitively indicates the number of numerical steps needed for computing a 0.2-s problem; and the step ratio of a FE model is its “# of steps to 0.2 s” divided by that of the SM-A. In addition, the computation time in each step depends on the matrix size ($3n \times 3n$) where n is the number of nodes in the 3rd column of Table 1.

Solved from Eq. (1) with the low-frequency assumption ($\beta = 0$) and a specified $\alpha = 180 \text{ s}^{-1}$, the simulated tip responses and maximum equivalent stresses of a 4.5-in. finger to an impulse load are compared in Fig. 6. Some observations can be made from Table 1 and Fig. 6:

- (1) All three simplified models yield similar results. However, for the same average element length of 4 mm, SM-C (Tetra) requires 3.21 times more steps than SM-A (Hexa) in computing a 0.2 s problem. It also takes 6.92 times more nodes (or 48 times larger matrix size) in each time-step. Also, SM-C has an average element length 2 times than that of SM-B (Refined Hexa) but needs a smaller time-step.
- (2) The complex geometry of the DM cannot be meshed with hexa elements as small features lead to highly nonhomogeneous element lengths. As the time-step is determined by the smallest element in the whole domain, this leads to a large number of steps (18.36 times larger than that of SM-A) needed to solve a 0.2 s problem. The actual computational time ratio of DM (relative to SM-A) is expected to be even larger than the step ratio because the matrix size in each step is in the order of n^2 ; the square of the matrix size ratio ($n_{\text{DM}}/n_{\text{SM-A}} = 34$) is over 1000.
- (3) For the same $\alpha = 180 \text{ s}^{-1}$, all three simplified models (SM-A, B, and C) yield similar over-damped tip responses and stress curves, but DM exhibits under-damped response as seen in Fig. 6(a). DM with $\alpha = 260 \text{ s}^{-1}$ gives a similar over-damped tip response but predicts lower stresses than the simplified models. This is because DM and SM have

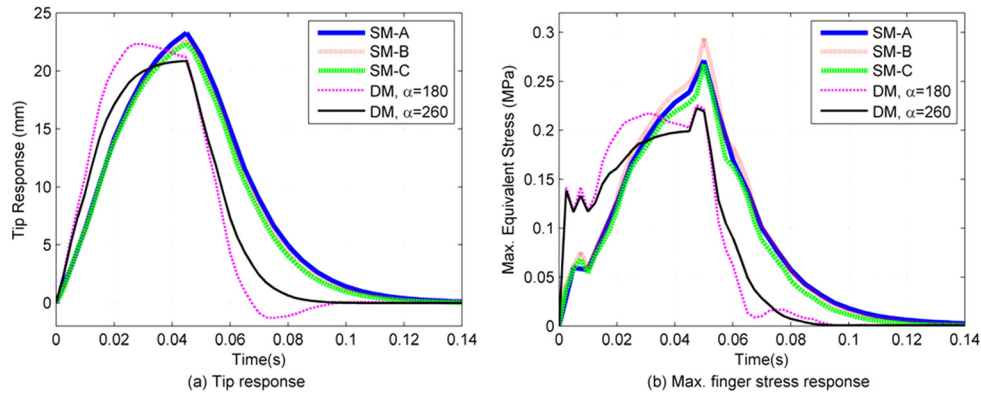


Fig. 6 Effect of FEA models (4.5-in. finger, $\alpha = 180 \text{ s}^{-1}$)

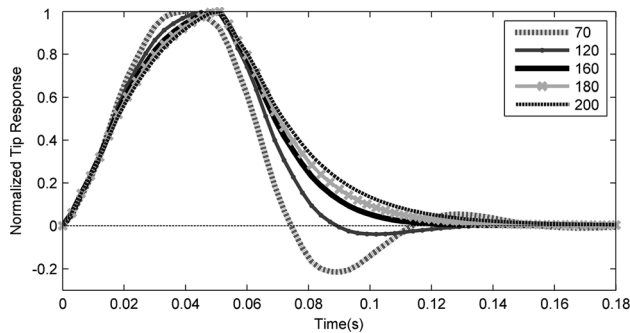


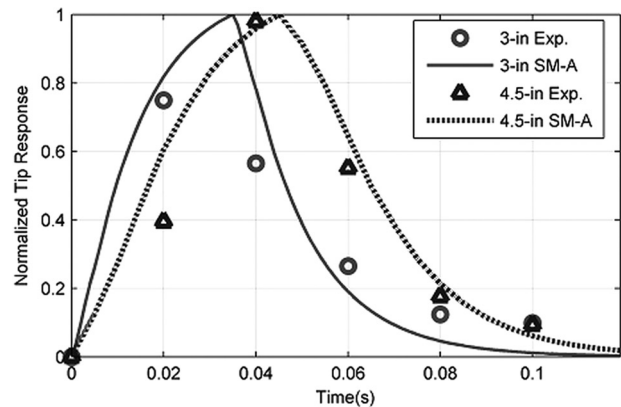
Fig. 7 Effect of α on tip response (4.5-in finger)

different geometries, and thus, different mass and stiffness matrices. As highlighted in the 1st column of Table 1, the simplified models have a 20% larger volume but an 8% lower stiffness (and hence, lower natural frequency) than the actual finger that has a stronger base, which accounts for the corresponding slower rise-time in their impulse responses.

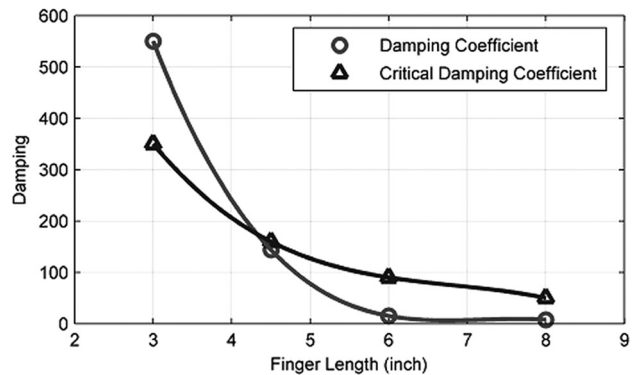
The simplified models overestimate the maximum deflection and stress (within 10%). These, along with the under-evaluated response time, suggest that the simplified models are reasonably conservative for a safe design. Based on the time-step study, SM-A which requires the smallest computational time is used in the dynamic simulation since the damping modeling is an iterative search procedure. Figure 7 illustrates the computed tip responses of the 4.5-in. finger to an impulse using SM-A model for five specified α values; 70, 120, 160, 180, and 200.

3.2 Damping Identification using Hybrid Experiment/Computation with SM-A. To illustrate the CCEDI procedure (Fig. 2), Eq. (1) with the SM-A is solved for the mass proportional coefficient α of four compliant fingers (3, 4.5, 6, and 8-in.). By comparing against the numerically computed α_{cr} for each finger, the experimentally obtained impulse response data using the setup shown in Fig. 5(b) fall into two categories:

- (1) *Under-damped*: The damping ratios of 6 and 8-in. fingers were experimentally determined from the log-decrement to be 0.17 and 0.15, respectively, and their corresponding damping coefficients ($\alpha = \zeta\alpha_{cr}$) are 15 s^{-1} and 7.5 s^{-1} .
- (2) *Over-damped*: By numerically searching for a match between simulation and experimentally obtained impulse response data, the α coefficients for 3 and 4.5-in. fingers were determined to be 600 s^{-1} and 180 s^{-1} , respectively. As compared in Fig. 8(a), the simulated and experimental tip responses agree acceptably well.



(a) Comparison (SM-A, 3 and 4.5-in fingers)



(b) Effect of finger length on damping

Fig. 8 Damping coefficients of compliant fingers

The above α and α_{cr} results are summarized in Fig. 8(b), and curve-fitted as a function of the finger length x in Eq. (7) and Eq. (8) by polynomial and power functions, respectively

$$\alpha = \begin{cases} 56.667x^2 - 705x + 2205 \\ -3.75x + 37.5 \end{cases} \quad \text{when } \begin{cases} 3 \leq x \leq 6 \\ 6 \leq x \leq 8 \end{cases} \quad (7)$$

$$\alpha_{cr} = 3120.4x^{-1.983} \quad \text{when } 3 \leq x \leq 8 \quad (8)$$

Based on these approximations, the damping parameters for these particular fingers with different lengths can be estimated.

3.3 Validation Against Previously Published Experimental Data. Figure 9(a) shows the setup designed to experimentally measure contact forces exerted on the fixed (aluminum) elliptical

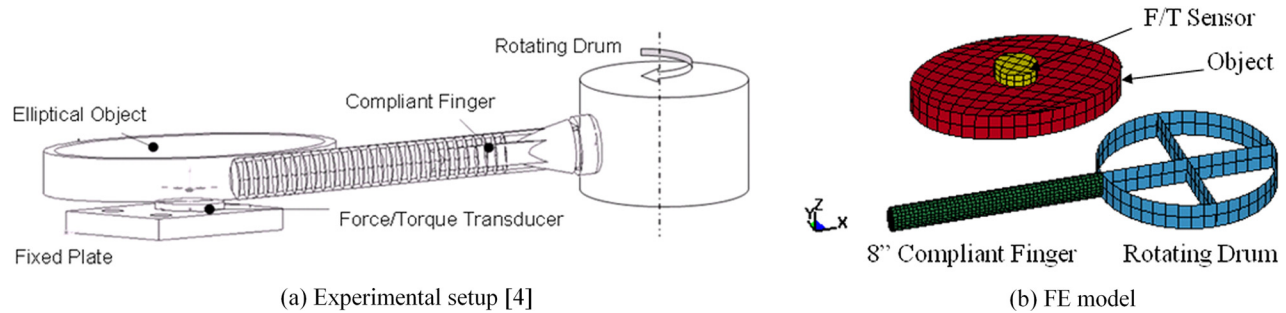


Fig. 9 Experiment Setup for simulating contact between rotating finger and elliptical object

Table 2 FE model and material properties

Part (Material)	Material properties			Dimensions (mm)	Element (ANSYS)		
	E (GPa)	ν	ρ (kg/m ³)		Type	Numbers	Nodes
Object (AL6061)	69	0.33	2700	99.1,67,3(25)	Solid 164	242	432
Drum (Steel)	210	0.28	7700	82.55 (25)	Shell 163	144	212
Finger (Rubber)	0.0061	0.49	1000	12,8.45,203.2	Solid 164	1275	1872
F/T sensor (AL6061)	69	0.33	2700	20(12.25)	Solid 164	32	75

Relative distance between object-center and drum-center = ($\Delta x=101.6$ mm, $\Delta y=184.15$ mm).

Constraints: Nodes along drum axis are fixed at U_x, U_y, U_z, R_x, R_y .

Drum rotating speed $\omega=20$ rpm (2.095 rad/s).

Friction coefficient between finger and drum $\mu=0.6$.

Mass proportional damping coefficient $\alpha=7.5$ s⁻¹.

object by a rotating 8-in. finger using a 6-DOF force/torque transducer. As shown in Fig. 9(a), the finger is oriented such that it deflects in the plane perpendicular to the rotating axis. The 3D FEA conducted here extends the 2D version in Ref. [4] where published experimental data are available for validation by taking into accounts the damping effects and relaxing the quasi-static assumption previously made.

Based on data given in Ref. [4], the geometry modeling, material properties, and friction coefficient between the rubber finger and aluminum object, boundary conditions, and the (ANSYS) element types/nodes for this study are summarized in Table 2 where element types and their transformations from ANSYS to LS-DYNA for solving the dynamic Eq. (1) using explicit time-integration are defined in Appendix B. Based on the time-step study described in Section 3.1, uniform hexagonal and quadrangular elements are used in this simulation. For the deformable contact involved in this dynamic problem, the load vector $\{F\}$ in Eq. (1) includes contact forces at the contact interface. The interaction between two bodies is modeled as a constraint condition that the two bodies cannot penetrate into each other using the penalty method built-in LS-DYNA [11]. The numerically predicted reaction force and deformed shapes (as the drum rotates the finger at a constant speed of 20 rpm passing over the stationary object) are compared in Figs. 10 and 11 against measurements [4] and experimentally captured snapshots at some specific instants, which show excellent agreement.

3.4 Effect of Damping on Reaction Forces and Stresses. As shown in Sections 3.1 and 3.2, the mass proportional damping coefficient α of a continuum structure depends on its geometrical shape and aspect (length-to-area) ratio for a specified material. To facilitate design analyses, it is desired to understand the effect of damping coefficients (for structures with similar mass and stiffness characteristics) on the contact-induced deflection and contact stress. Six different α values ($\alpha=1, 7.5, 20, 50, 180,$ and 600 s⁻¹ correspond to damping ratios of $\zeta=0.02, 0.15, 0.4, 1, 3.6,$ and $12,$ respectively) were studied for the experimental setup (Fig. 9(a)). The values of all other parameters needed for

the simulation are given in Table 2. Simulated snapshots graphically illustrating the effects of damping coefficients on the finger deflection and contact locations as the drum rotates at a constant speed are shown in Figs. 12 and 13. While rotating, the compliant finger exerts a contact force on the elliptical object. Figures 14(a) and 14(b) graph the maximum equivalent stress of the finger and object, respectively. As known as Von Mises stress, the equivalent stress defined in Eq. (9) is a general interpretation to account for the complex combination of tension, compression, bending, and torsion:

$$\sigma_{\text{equivalent}} = \sqrt{\frac{(\sigma_1 - \sigma_2)^2 + (\sigma_2 - \sigma_3)^2 + (\sigma_3 - \sigma_1)^2}{2}} \quad (9)$$

The maximum reaction forces simulating the sensor measurement are compared in Fig. 14(c). The observations from Figs. 12 to 14 are divided into three regions; before, during and after contact:

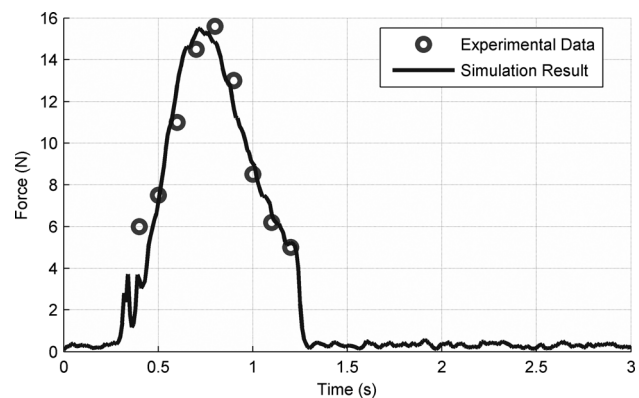


Fig. 10 Reaction force from the contact between rotating finger and elliptical object

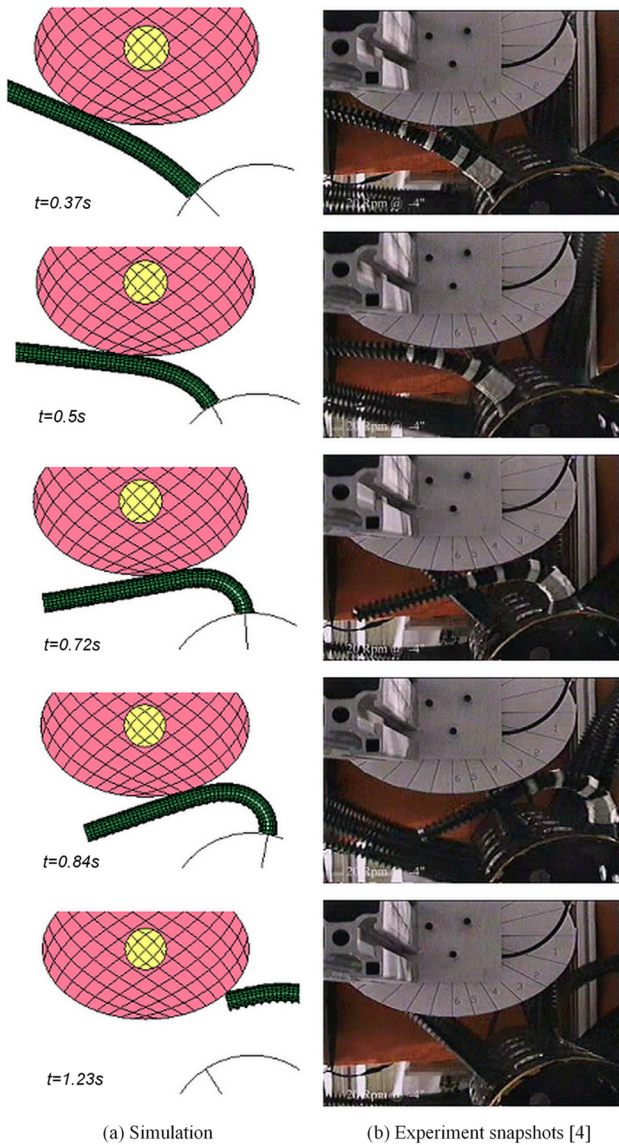


Fig. 11 Simulation and experimental results of finger-contact deformation

Before Contact: The finger deforms and its maximum stress rises sharply (Figs. 12 and 14(a)) for the highly damped cases ($\alpha = 180$ and 600 s^{-1}) as the drum rotates at a constant speed. If unobstructed, its stress curve would continue to rise exponentially to a steady-state value dependent on the damping coefficient and rotating speed. The maximum finger stress (at the fixed end) increases with the damping coefficient.

During Contact: The initial deflection (just before contact) has a significant effect on the timing and location at which the finger initially contacts the object as illustrated in Fig. 13(a):

- Figure 13(a) shows that the finger with a relatively low damping coefficient ($\alpha = 7.5 \text{ s}^{-1}$) experiences negligible deformation before contacting the *front* side of the elliptical object at $t = 0.32 \text{ s}$. The finger with very high damping coefficient ($\alpha = 600 \text{ s}^{-1}$) drastically deforms causing the initial contact to occur on the *rear* side of the elliptical object at $t = 0.57 \text{ s}$ (a $1/4$ second later than the finger with $\alpha = 7.5 \text{ s}^{-1}$).
- The finger and object exhibit nearly identical stress responses and reaction force before reaching its maximum stress as shown in Figs. 14(a)–14(c), after which the stress/deflection relaxation of the finger depends on its damping coefficient. This, along with the observations that the three fingers ($\alpha = 7.5, 180, \text{ and } 600 \text{ s}^{-1}$) breakaway from the

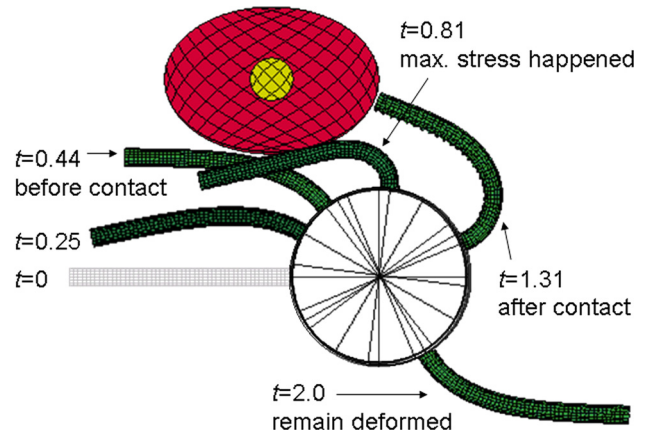
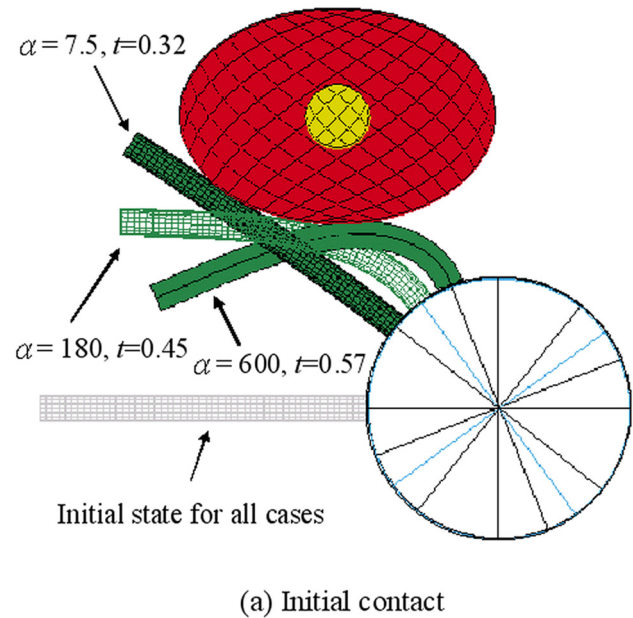
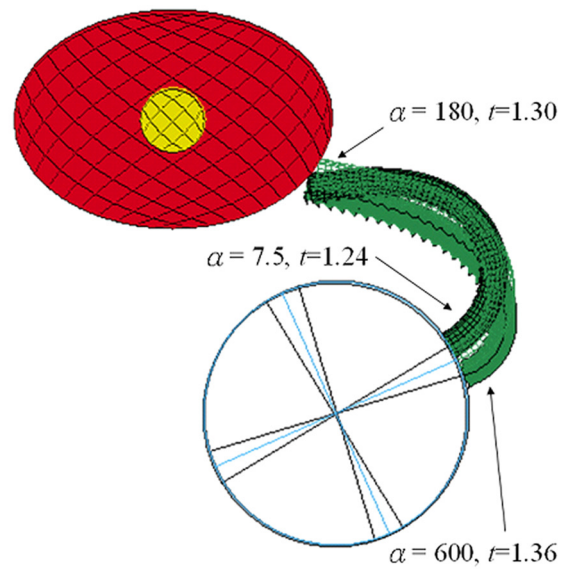


Fig. 12 Simulated snapshots illustrating the finger deformation ($\alpha = 180 \text{ s}^{-1}$)



(a) Initial contact



(b) Final contact

Fig. 13 Initial and final contact ($\alpha = 7.5, 180 \text{ and } 600 \text{ s}^{-1}$)

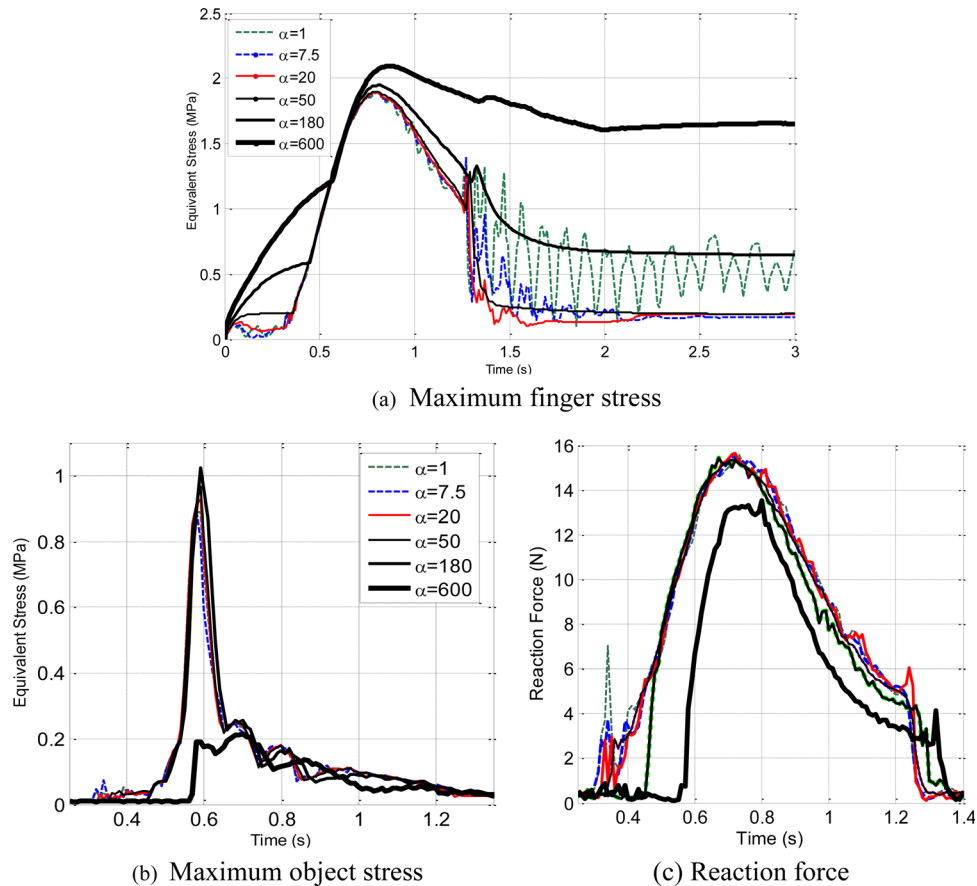


Fig. 14 Effect of finger damping coefficient on maximum finger/object stresses and reaction force

object at the same location as shown in Fig. 13(b), implies that the contact-constrained finger deflection primarily depends on the object shape and finger stiffness; these findings are consistent with the reporting in Ref. [4], and imply that the damping effect is not significant in this specific case. In other words, the quasi-static assumption may be made “during contact” for this particular case except for the extra-high damped finger ($\alpha = 600 \text{ s}^{-1}$).

- Higher damping results in a longer settling time from its initial deformation. As shown in Figs. 14(b) and 14(c), the finger with $\alpha = 600 \text{ s}^{-1}$ exerts a smaller force on (and hence induces a lower stress in) the object than the finger with a lower damping.
- As shown in Fig. 13, the contact duration decreases as the damping coefficient increases. For this specified elliptical object, the contact duration of these three fingers with $\alpha = 7.5, 180,$ and 600 s^{-1} are 0.92 s, 0.85 s, and 0.79 s, respectively.

After Contact: Maximum stresses in the high-damped fingers (with $\alpha = 180$ and 600 s^{-1}) which remain deformed decay without overshoot to their steady-state values (Fig. 14(a)). On the other hand, the low-damped finger vibrates naturally once released from its deflection. Vibratory fingers are undesirable when used in handling live products (such as live broilers for poultry meat processing) as their reactions could result in handling damage. The above findings suggest that the choice of damping coefficients is a trade-off among several design considerations including contact location, duration, and stresses/forces on the object as well as suppression of oscillatory responses to minimize natural reflexes of live products being handled.

4 Conclusion

A coupled computational and experimental damping identification (CCEDI) procedure has been introduced to determine the damping coefficients for FEA, and account for its effects on the contact exerted by a rotating compliant finger on an object. Experimentally validated against published data, this CCEDI procedure relaxes several limitations of traditional damping identification methods (such as log-decrement and half-power methods) commonly used to determine the damping ratio from an oscillatory response for lump-parameter analyses. This method can be used to obtain the damping coefficients from both oscillatory and non-oscillatory responses for FEA, and analyze highly damped continuum structures. Practical issues encountered in implementing the coupled procedure using LS-DYNA with a built-in penalty method to handle deformable contacts have been investigated for low-frequency applications where Rayleigh damping reduces to a single term proportional to the mass matrix. Numerical investigation on contact exerted by a rotating finger demonstrates that damping coefficients play an important role on the initial deflection before contact, and thus, the timing and location of the contacts. Although it has been illustrated in the context of a compliant finger, the procedure presented here can be extended to analyze other flexible multibody dynamic problems involving large deformable contact without neglecting the damping effects.

Acknowledgment

This project was jointly funded by the Agricultural Technology Research Program, the US Poultry and Eggs Association, and the Georgia Food Industry Partnership.

Table 3 General element types for explicit dynamic FEA

ANSYS element type	BEAM 161	SHELL 163	SOLID 164	MASS 166	SOLID 168
Element plot					
Equivalent in LS-DYNA	Beam #1	Shell #2	Solid #1	Mass	Solid #16
Number of nodes	2	4	8	1	10
DOFs per nodes	12	12	9	9	3
DOF (where $i=x, y, z$)	U_i, V_i, A_i, R_i	U_i, V_i, A_i, R_i	U_i, V_i, A_i	U_i, V_i, A_i	U_i

Appendix A: Formulation of Dynamic FEM

For a single-element subject to the body force $\{f\}$, surface traction $\{\tau\}$ and concentrated load $\{p\}$, the work balance on the element (with volume Ω , surface Γ , density ρ and viscous damping coefficient c) is given by Eq. (A1)

$$\int_{\Omega} \{\delta u\}^T \{f\} dv + \int_{\Gamma} \{\delta u\}^T \{\tau\} ds + \sum_{i=1}^n \{\delta u\}_i^T \{p\}_i = \int_{\Omega} [\{\delta u\}^T \rho \{\ddot{u}\} + \{\delta u\}^T c \{\dot{u}\} + \{\delta \epsilon\}^T \{\sigma\}] dv \quad (A1)$$

In Eq. (A1), the right-hand side accounts for the effects due to inertia, viscosity, and strain energy, respectively; and $\{\delta u\}$ and $\{\delta \epsilon\}$ are the virtual displacement and its corresponding strain.

In FE formulation where physical phenomena are analyzed in discrete domains, the displacement $\{u\}$ in (A1) is a function of space and time, and represented by interpolating functions and nodal DOF, $\{u\} = [N]\{x\}$ where $[N]$ is a space-dependent interpolation function matrix based on the element types; and $\{x\}$ is the nodal DOF dependent on time only. Using the constitutive equations

$$\{\epsilon\} = [B]\{x\} \quad (A2a)$$

$$\{\sigma\} = [E]\{\epsilon\} = [E][B]\{x\} \quad (A2b)$$

where $[B]$ and $[E]$ are the strain-displacement and stress-strain matrixes. Equation (A1) can be written in terms of external load $\{r_{ext}\}$, and element mass, damping, and stiffness matrixes (respectively, denoted as $[m]$, $[c]$, and $[k]$)

$$[m]\{\ddot{x}\} + [c]\{\dot{x}\} + [k]\{x\} = \{r_{ext}\} \quad (A3)$$

where

$$[m] = \int_{\Omega} \rho [N]^T [N] dv \quad (A3a)$$

$$[c] = \int_{\Omega} c [N]^T [N] dv \quad (A3b)$$

$$[k] = \int [B]^T [E] [B] dV \quad (A3c)$$

and

$$\{r_{ext}\} = \int_{\Omega} [N]^T \{f\} dv + \int_{\Gamma} [N]^T \{\tau\} ds + \sum_{i=1}^n \{p\}_i \quad (A3d)$$

The computational model for the system can be derived by assembling (A3) over the whole domain to be analyzed, which leads to Eq. (1).

Appendix B: Description of Element Types in General Explicit Dynamic FEA

The elements types [15] used in this study are summarized in Table 3, which shows the transformation relation between ANSYS and LS-DYNA, node number for each specific element, and the DOF (displacement U , velocity V , acceleration A , rotation R , and x, y, z directions). In Table 3, BEAM161 is a line element defined by 2 nodes and the beam cross-section; SHELL163 is a 4-node shell element with bending and membrane capabilities (where in-plane and normal loads are both permitted); SOLID164 (preferred for the 3D explicit dynamic FEA for time-step considerations) is a hexahedral element used for the solid structures; MASS166 is defined by a single node with concentrated mass; and SOLID168 (useful in modeling 3D complex geometry imported from CAD packages) is a 3D higher-order 10-node tetrahedral element and has a quadratic displacement behavior.

References

- [1] Lee, K.-M., 2001, "Design Criteria for Developing an Automated Live-Bird Transfer System," *IEEE Trans. Rob. Autom.*, **17**(4), pp. 483–490.
- [2] Howell, L. L., Midha, A., and Norton, T. W., 1996, "Evaluation of Equivalent Spring Stiffness for Use in a Pseudo-Rigid-Body Model of Large-Deflection Compliant Mechanisms," *ASME J. Mech. Des.*, **118**, pp. 126–131.
- [3] Midha, A., Howell, L. L., and Norton, T. W., 2000, "Limit Positions of Compliant Mechanisms Using the Pseudo-Rigid-Body Model Concept," *Mech. Mach. Theory*, **35**, pp. 99–115.
- [4] Lee, K.-M., Joni, J., and Yin, X., 2001, "Compliant Grasping Force Modeling for Handling of Live Objects," *ICRA2001*, May 21–26, Seoul, Korea, pp. 1059–1064.
- [5] Lan, C.-C., and Lee, K.-M., 2008, "An Analytical Contact Model for Design of Compliant Fingers," *ASME J. Mech. Des.*, **130**, p. 011008.
- [6] Li, Q., and Lee, K.-M., 2008, "An Adaptive Meshless Method for Modeling Large Mechanical Deformation and Contacts," *ASME J. Appl. Mech.*, **75**(4), p. 041014.
- [7] Pagnini, L. C., and Solari, G., 2001, "Damping Measurements of Steel Poles and Tubular Towers," *Eng. Struct.*, **23**(9), pp. 1085–1095.
- [8] Zhu, Z. H., and Meguid, S. A., 2007, "Nonlinear FE-Based Investigation of Flexural Damping of Slacking Wire Cables," *Int. J. Solids Struct.*, **44**(16), pp. 5122–5132.
- [9] Drew, S. J., and Stone, B. J., 2002, "Torsional Damping of a Back-to-Back Gearbox Rig: Experimental Measurements and Frequency Domain Modeling," *Proc. Inst. Mech. Eng. Part K: J. Multibody Dyn.*, **216**, pp. 157–168.
- [10] Low, K. H., Wang, Y., Hoon, K. H., and Vahdati, N., 2004, "Initial Global-Local Analysis for Drop-Impact Effect Study of TV Products," *Adv. Eng. Software*, **35**(3–4), pp. 179–190.
- [11] LS-DYNA Theory Manual (compiled by J. O. Hallquist), 2006, Livermore Software Technology Corporation.
- [12] Cook, R. D., Malkus, D. S., Plesha, M. E., and Witt, R. J., 2001, *Concepts and Applications of Finite Element Analysis*, 4th ed., Wiley, New York.
- [13] Yoo, W.-S., Lee, J.-H., Park, S.-J., Sohn, J.-H., Dmitrochenko, O., and Pogorelov, D., 2003, "Large Oscillations of a Thin Cantilever Beam: Physical Experiments and Simulation Using the Absolute Nodal Coordinate Formulation," *Nonlinear Dyn.*, **34**, pp. 3–29.
- [14] Mullen, R., and Belytschko, T., 1983, "An Analysis of an Unconditionally Stable Explicit Method," *Comput. Struct.*, **16**(6), pp. 691–696.
- [15] ANSYS Element Reference, Release 12, ANSYS Inc.